THE JOURNAL OF PHYSICAL CHEMISTRY C
A JOURNAL OF THE AMERICAN CHEMICAL SOCIETY

pubs.acs.org/JPCC

Article

Thermally Tunable Adsorption of Xenon in Crystalline Molecular Sorbent

Published as part of The Journal of Physical Chemistry virtual special issue "Marsha I. Lester Festschrift".

Kang Du and Ivan J. Dmochowski*

Cite This: *J. Phys. Chem. C* 2023, 127, 13810−13816

Read Online

ACCESS | Metrics & More | Article Recommendations | Supporting Information

ABSTRACT: The thermostability of encapsulated xenon is investigated in a series of isostructural crystalline sorbents. These sorbents consist of metal−organic capsules, with the general formula of $[Co_nFe_{4-n}L_6]^{4-}$ (n = 1, 2, 3, and 4), where L^{2-} is an organic linker with two sulfonate groups. In the crystalline sorbent, guanidinium cations form H-bond networks with the peripheral sulfonate groups in the solid state and trap xenon in the molecular cavities, which are at least 2.7 times the volume of xenon. When heated, the sorbent retains xenon up to 561 K, i.e., 396 K higher than the boiling point of xenon. Furthermore, the thermostability of trapped xenon can be modulated by varying the ratio of Co:Fe in the crystalline sorbent. Elemental analysis on a single crystal by energy dispersive X-ray spectroscopy confirms the homogeneous distribution of Co and Fe in the sorbent. Structural analyses reveal that the expansion of capsule cavity is proportional to the Co:Fe ratio, with increases of 0.049(1) Å and 6.4(8) Å^3 in metal−metal distance and cavity volume, per substitution of Fe by Co center. Steric repulsion between peripheral sulfonate groups is found to render a hypothetical face-centered cubic structure of $(C(NH_2)_3)_4[Fe_4L_6]$ not accessible, which would have trapped xenon with exceptional thermostability. The stable and tunable trapping of xenon in crystalline sorbents by oversized molecular cavities suggests a new strategy for separation and storage of xenon, through introduction of kinetic barriers, such as H-bond networks.

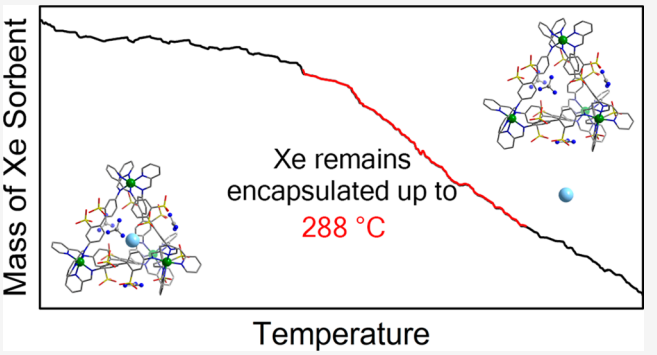

INTRODUCTION

The noble gas xenon (Xe) plays myriad roles in modern science, engineering, and medicine, and the applications are growing in many areas. Over 9 tons of xenon are consumed annually for medical purposes, mostly for its use as a volatile, nontoxic general anesthetic.[1,2] Emerging imaging modalities with xenon will further increase the demand of xenon in medical fields.[3−5] Modern space exploration also fuels the demand for xenon by employing large quantities of xenon for spacecraft ion propulsion.[6] Nowadays, xenon is collected as a byproduct from air distillation plants.[7,8] A second cryogenic distillation is required to separate xenon from other noble gases, which is energetically expensive and limits the current supply. On the other hand, stable isotopes of xenon in gaseous nuclear waste impose unnecessary volumetric cost for disposal, which is commonly achieved by burial in deep geological repositories.[9] Extracting stable isotopes of xenon will both lower the costs for nuclear waste disposal and provide an additional source of xenon production.[10] Thus, selective sorbents for xenon that operate at near-ambient conditions, such as atmospheric pressure and room temperature, will be highly desirable for the production, storage, and even recycling of xenon.

Extended solid materials, such as carbon-based solids,[11−14] zeolites,[15−17] and metal−organic frameworks (MOFs),[18−22] have been explored as xenon sorbents. Surface residues, such as hydrogen-bonding groups,[23,24] polar substituents,[25] unsaturated metal sites,[26,27] and nanostructures,[28,29] have been incorporated to induce favorable gas−surface interactions and improve selectivity. Recently, MOFs with small pores comparable to the diameter of xenon (~4.3 Å)[30] showed considerable promise for kinetic separation, as the pores selectively retain xenon over other smaller gases.[14,18] Extended solids certainly represent a class of promising xenon sorbents. But understanding how a large ensemble of xenon atoms interacts with an extended surface can be complicated and oftentimes involves sophisticated theoretical modeling. Toward this end, experimental studies on discrete molecular

Received: March 28, 2023
Revised: June 20, 2023
Published: July 10, 2023

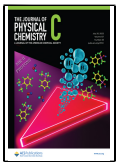

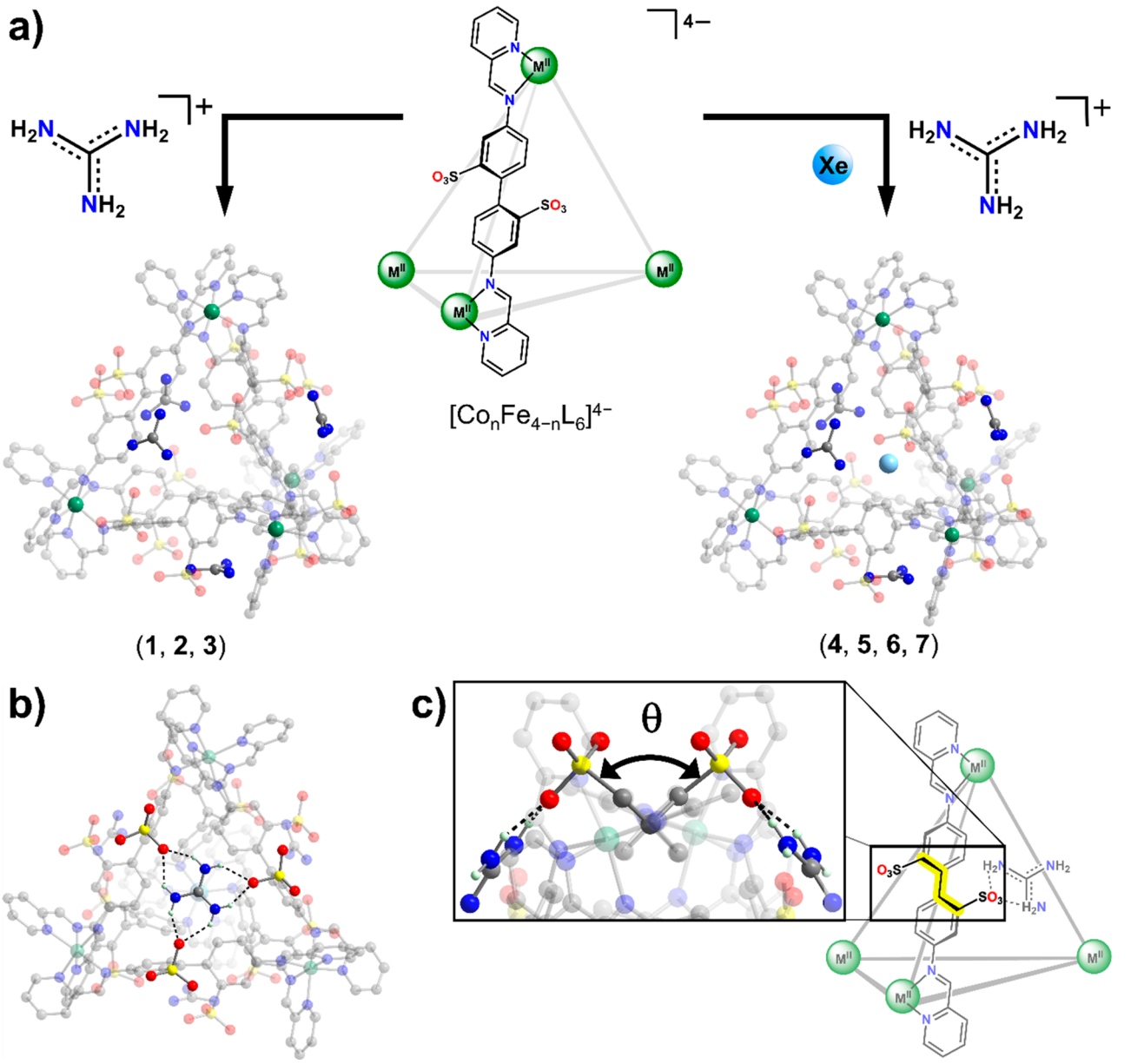

Figure 1. (a) Preparations of heterobimetallic capsules and the corresponding Xe-entrapped molecular crystals. (b) Representative demonstration of the six H-bonds formed between $(C(NH_2)_3)^+$ and interfacial sulfonate groups on each facet of Co_nFe_{4-n} tetrahedra, as observed in **1**−**7**. (c) Chemical structure of the $(C(NH_2)_3)^+$-capped M^{II}_4 capsules in the solid state and illustration of the dihedral angle $\angle C_{sulfonate}CC'C'_{sulfonate}$ (θ). Gray, blue, red, yellow, dark green, and light blue spheres represent C, N, O, S, Fe/Co (M^{II}), and Xe atoms, respectively. H atoms are omitted for clarity except for those participating in H-bonding, which are represented by light green spheres.

capsules can provide complementary understanding of xenon−host interactions on a molecular level.

Crystalline solids formed by molecular capsules with well-defined cavities and well-characterized xenon−host interactions have also shown great promise as xenon sorbents. These capsules can adsorb gas with permanent porosity in the solid state[31] or encapsulate xenon in solution.[32−38] Synthetic optimization of the cavity volume and shape can result in very stable xenon−host complexes. For example, xenon was stably trapped in a trigonal crystal of cryptophane-111 to a temperature as high as 563 K.[34] Such high thermostability was attributed to both the high xenon affinity of cryptophane-111 and intermolecular blockage of cavitand portals due to molecular packing. This was evidenced by the 180 K lower xenon dissociation temperature in another triclinic phase of cryptophane-111, where the cavitand portals were not hindered.[34] As such, crystal packing can be as influential as molecular design in determining the stability of the entrapped gases in molecular sorbents.

Self-assembled metal−organic capsules with the general formula $[Co_nFe_{4-n}L_6]^{4-}$, where L^{2-} = 4,4′-bis[(2-pyridinylmethylene)amino][1,1′-biphenyl]-2,2′-disulfonate and n = 0−4, were found to encapsulate xenon in solution[39−41] and solid state (Figure 1a). Sequential substitution of each Fe^{II} cation by high-spin Co^{II} afforded incremental increase in xenon exchange rate in aqueous solutions, up to 40-fold in $[(Xe)Co_4L_6]^{4-}$ as compared to its all-Fe^{II} congener.[39] Importantly, in the presence of guanidinium, $(C(NH_2)_3)^+$, the xenon−host complex $[(Xe)Co_nFe_{4-n}L_6]^{4-}$ can be readily crystallized under atmospheric pressure of xenon. Each facet of

https://doi.org/10.1021/acs.jpcc.3c02054
J. Phys. Chem. C 2023, 127, 13810−13816

the $[(Xe)Co_nFe_{4-n}L_6]^{4-}$ tetrahedron was capped by one $(C(NH_2)_3)^+$ cation, which formed six nearly symmetric H-bonds with three interfacial sulfonate groups, thereby sterically blocking the exit of xenon (Figure 1b).[40,41] While crystallizing guest-free $[Co_4L_6]^{4-}$ was not feasible as shown in previous studies,[42] the guest-free and xenon-encapsulated isostructures can be achieved in heterobimetallic $[Co_nFe_{4-n}L_6]^{4-}$ capsules, where low-spin Fe^{II} centers stabilize the guest-free capsules.[41]

Xenon atoms were stably trapped in crystalline solids beyond the time scale of structural analyses in previous studies,[40,41] especially considering that the molecular cavities (>115 Å^3) were much larger than the volume of xenon atoms (~42 Å^3). Herein we investigated the tunable $(C(NH_2)_3)^+$-assisted encapsulation of xenon in a series of isostructural Co_nFe_{4-n} molecular sorbents with varying Co^{II}:Fe^{II} stoichiometries. We explored the structural features that allowed formation of the face-centered cubic phase in which all facets of $[M^{II}_4L_6]^{4-}$ were capped by $(C(NH_2)_3)^+$, in the absence and presence of xenon. Having a consistent isostructural system, we elucidate how subtle composition changes, reflected by the Co^{II}:Fe^{II} content, can substantially influence the empirical structure and subsequently modulate the dissociation temperature of xenon.

EXPERIMENTAL METHODS

General Considerations. Unless otherwise specified, chemicals and solvents were purchased from commercial vendors and used without purification. Deuterated solvents were purchased from Cambridge Isotope Laboratories and Sigma-Aldrich. Water was obtained from an EMD Millipore purification system. Naturally abundant Xe gas (99.995%) was purchased from the Linde Group. Anhydrous 4,4′-diaminobiphenyl-2,2′-disulfonic acid was prepared by evacuating the commercial product (containing at most 30% H_2O) in dynamic vacuum (<4 Pa) at 393 K for 48 h. Picolinaldehyde (PA) was purified via distillation at 313 K under dynamic vacuum (<4 Pa) prior to use. Preparations of $(C(NH_2)_3)_4[Co_{1.8}Fe_{2.2}L_6]\cdot 69H_2O$ (**2**), $(C(NH_2)_3)_4[Co_{2.7}Fe_{1.3}L_6]\cdot 73H_2O$ (**3**), $(C(NH_2)_3)_4[(Xe)_{0.8}Co_{1.8}Fe_{2.2}L_6]\cdot 69H_2O$ (**5**), and $(C(NH_2)_3)_4[(Xe)_{0.7}Co_4L_6]\cdot 75H_2O$ (**7**), where L^{2-} = 4,4′-bis[(2-pyridinylmethylene)amino][1,1′-biphenyl]-2,2′-disulfonate, were synthesized according to reported procedures.[40,41]

Elemental Analysis of Bulk Compounds. The S, Fe, and Co content of bulk compounds was determined by inductively coupled plasma optical emission spectroscopy (ICP-OES), using a Spectro Genesis ICP-OES instrument. Samples were digested and diluted in 3% (v/v) HNO_3 such that the final concentrations for S, Fe, and Co were approximately 165, 75−25, and 25−75 ppm, respectively, prior to measurements. The concentrations of each element were calculated and generated by the operating program by linear regression. The Co/Fe ratios were obtained by directly taking the ratios between the concentrations for Co and Fe.

Elemental Analysis of Single Crystals. The S, Fe, and Co contents of single crystal samples were determined by energy dispersive X-ray spectroscopy (EDX), using a JEOL 7500F scanning electron microscope with an EDAX Octane Elect detector and an accelerating voltage of 15 kV. In a typical experiment, a crystalline solid suspended in isopropanol was drop-cast onto an Al sample holder prior to measurements. The data were analyzed using the APEX software package.

Thermostabilities of Encapsulated Xe Compounds. The thermostabilities of compounds were examined by thermogravimetric analysis followed by gas-phase mass spectrometry (TGA-MS), using a NETZSCH STA F3 Jupiter instrument coupled with GC−MS. In a typical experiment, 10−20 mg of solid was placed in an Al crucible, which was then heated from 303 to 773 K with a 5 K/min ramp rate under a He atmosphere. The mean dissociation temperatures for xenon, T_m, were calculated by the following formula,

$$T_m = \sum (\mathrm{Abs}_i T_i) / \sum (\mathrm{Abs}_i)$$

where Abs_i is the MS intensity at m/z = 131 (atomic mass for most abundant ^{131}Xe isotope) that was measured at temperature T_i.

X-ray Structural Analyses. Single crystals of **1**, **4**, and **6** were directly coated with Paratone-N oil and mounted on CryoLoop rods. The crystallography data for **1**, **4**, and **6** were collected on a Bruker APEXII CCD area detector, employing graphite-monochromated Mo Kα radiation (λ_{Mo} = 0.71073 Å) at 100 K. Rotation frames were integrated using SAINT,[43] producing a listing of unaveraged F^2 and $\sigma(F^2)$ values. The intensity data were corrected for Lorentz and polarization effects and for absorption using SADABS.[44,45] The structures were solved by the direct method using SHELXT and refined by SHELXL[46] within the OLEX2 interface.[47,48] The internal volumes in **1**, **4**, and **6** were estimated by SQUEEZE within the OLEX2 interface (shown as "solvent mask" function).[49] Detailed crystallographic analyses, disordered solvent molecules, and refinement data can be found in the Supporting Information and are listed in Table S1. All hydrogen atoms were placed at calculated positions using suitable riding models and refined using isotropic displacement parameters derived from their parent atoms. Thermal parameters for all non-hydrogen atoms were refined anisotropically. The solvent mask procedure as implemented in OLEX2 was applied to the structures of **1**, **4**, and **6** to account for severely disordered H_2O molecules that could not be properly modeled. A total of 5312, 5405, and 5828 electrons were found in solvent accessible void volumes of 16675, 16670, and 16779 Å^3 per unit cell in the crystal structures of **1**, **4**, and **6**, respectively. These electron densities were ascribed to 66, 68, and 73 H_2O molecules for each $[Co_nFe_{4-n}L_6]^{4-}$ unit in the structures of **1**, **4**, and **6**, respectively. The occupancies of encapsulated Xe atoms were freely refined to give 0.8 and 0.7 Xe in structures **4** and **6**.

Preparation of Stock Mixtures of Co_nFe_{4-n} Molecules ($\{Co_nFe_{4-n}L_6\}$). The preparations of solid stocks of $\{Co_nFe_{4-n}L_6\}$ were based on the reported procedure.[40] Mixtures of 1:3 and 3:1 equiv of $CoSO_4\cdot 7H_2O$:$FeSO_4\cdot 7H_2O$ were used in the syntheses to afford empirical mixtures of $\{CoFe_3L_6\}$ and $\{Co_3FeL_6\}$.

Preparation of $(C(NH_2)_3)_4[Co_{0.9}Fe_{3.1}L_6]\cdot 66H_2O$ (1). An aqueous solution (18 mL) of about 5 mM $\{CoFe_3L_6\}$ was filtered and transferred to a test tube. One aliquot of 2 M $(C(NH_2)_3)_2SO_4$ (1.8 mL) was injected to the bottom of the test tube via a Hamilton syringe. The test tube was capped by a rubber septum and left to stand for 2 weeks to yield dark purple crystals of $(C(NH_2)_3)_4[Co_{0.9}Fe_{3.1}L_6]\cdot 66H_2O$ (**1**), which was suitable for X-ray structural analysis. Crystallographic data are summarized in Table S1. The yield of **1** was 69%. The Co:Fe ratio was determined by ICP-OES.

Preparation of $(C(NH_2)_3)_4[(Xe)_xCo_nFe_{4-n}L_6]\cdot yH_2O$. The preparations of xenon-encapsulated crystals were based on reported procedures.[40,41] $\{CoFe_3L_6\}$ and $\{Co_3FeL_6\}$ were used

https://doi.org/10.1021/acs.jpcc.3c02054
J. Phys. Chem. C 2023, 127, 13810−13816

as starting materials to yield dark purple crystals of $(C(NH_2)_3)_4[(Xe)_{0.8}Co_{1.0}Fe_{3.0}L_6]\cdot 68H_2O$ (**4**) and $(C(NH_2)_3)_4[(Xe)_{0.7}Co_{2.7}Fe_{1.3}L_6]\cdot 73H_2O$ (**6**), which were suitable for X-ray structural analyses. Crystallographic data are summarized in Table S1. The respective yields for **4** and **6** were 83% and 62%. Co:Fe ratios were determined by ICP-OES.

RESULTS AND DISCUSSION

The preparations of guest-free and xenon-encapsulated molecular crystals $(C(NH_2)_3)_4[Co_{1.8}Fe_{2.2}L_6]\cdot 69H_2O$ (**2**) and $(C(NH_2)_3)_4[Co_{2.7}Fe_{1.3}L_6]\cdot 73H_2O$ (**3**), $(C(NH_2)_3)_4[(Xe)_{0.8}Co_{1.8}Fe_{2.2}L_6]\cdot 69H_2O$ (**5**), and $(C(NH_2)_3)_4[(Xe)_{0.7}Co_4L_6]\cdot 75H_2O$ (**7**) were reported in previous studies.[40,41] Following similar procedures, $C(NH_2)_3)_4[Co_{0.9}Fe_{3.1}L_6]\cdot 66H_2O$ (**1**), $(C(NH_2)_3)_4[(Xe)_{0.8}Co_{1.0}Fe_{3.0}L_6]\cdot 68H_2O$ (**4**), and $(C(NH_2)_3)_4[(Xe)_{0.7}Co_{2.7}Fe_{1.3}L_6]\cdot 73H_2O$ (**6**) were prepared (Figure 1a) for a systematic investigation in the current study. Structural data are summarized in Table S1. This series of compounds consists of three pairs of guest-free and xenon-encapsulated sorbents with Co^{II}:Fe^{II} ratios of 1:3 (**1** and **4**), 2:2 (**2** and **5**), and 3:1 (**3** and **6**). Crystallization of guest-free $[Co_4L_6]^{4-}$ capsule was unsuccessful due to the lability of high-spin Co^{II}.[42] Crystallization of $[Fe_4L_6]^{4-}$ in the presence of $(C(NH_2)_3)^+$ resulted in a different crystallographic phase, in which only one facet of the capsule was capped by the H-bonding network.[50] The structural reason will be explained in detail in the following sections.

Crystalline compounds **1**−**7** are isostructural and adopt a face-centered cubic space group, $Fd\bar{3}$. The exact Co:Fe content in each compound was determined by ICP-OES. The almost identical Co:Fe ratios between the guest-free and xenon-trapped congeners (**1** and **4**, **2** and **5**, and **3** and **6**) suggest that encapsulation of xenon induces a negligible influence on the composition of the crystalline materials. In the structures for **1**−**7**, each facet of the tetrahedral $[Co_nFe_{4-n}L_6]^{4-}$ molecules is capped by one $(C(NH_2)_3)^+$ cation, which forms six H-bonds with interfacial sulfonate groups (Figure 1a). All metal centers are crystallographically equivalent, and each metal center is coordinated by three iminopyridyl moieties, residing in a distorted octahedral environment. Because the Co−N bond is longer than Fe−N (Co^{II} is high-spin, while Fe^{II} is low-spin), both M···M distances and internal volumes increase monotonically with increasing Co content, spanning the ranges of 12.875−12.981 Å and 115.5−129.8 $Å^3$, respectively (solid circles and empty diamonds in Figure 2). This observation suggests that the average cavity volume can be tuned by simple "doping" with Fe^{II} or Co^{II} centers. The respective increases in M···M distance and internal volume are 0.049(1) Å and 6.4(8) $Å^3$ per substitution of Fe^{II} by Co^{II}. The presence of xenon has a negligible influence on the M···M distances and internal volumes, as evidenced by the nearly superimposable trends for both the guest-free and xenon-bound congeners (Figure 2). This is attributed to the much larger cavities in **1**−**7**, which are 2.7−3.1 times greater than the volume of a xenon atom (~42 $Å^3$) and additional constraints from the H-bond networks induced by $(C(NH_2)_3)^+$.

The dihedral angle $\angle C_{sulfonate}CC'C'_{sulfonate}$, which is denoted as θ, bridges two neighboring $(C(NH_2)_3)^+$ molecules and appears to influence the formation of the $Fd\bar{3}$ crystal phase (Figure 1c). As summarized in Table 1, the angles θ for structures **1**−**7** fall in a small range (86.3−90.4°) and are approximately proportional to the Co content (Table 1). By comparison, the structure for $(C(NH_2)_3)_4[Fe_4L_6]$, where only one facet is capped by $(C(NH_2)_3)^+$, shows two θ values, 88.6(2) and 95.5(2)° for the atoms that participate in and lack H-bonding, respectively.[50] The association of the first $(C(NH_2)_3)^+$ cation likely renders θ on other sulfonates not suitable to accommodate additional $(C(NH_2)_3)^+$ molecules. This hypothesis is consistent with the shorter Fe−N bond length compared to Co−N, leading to more contracted and rigid portals in Fe_4L_6 capsules. The fact that compounds **1**−**7** afford the desired all-facet-capped structures is attributed to the structural flexibility introduced by the high-spin Co^{II} centers. The upper limit for θ that allows for H-bonding with $(C(NH_2)_3)^+$ can be estimated to reside between 90.4(7) and 95.5(2)° (Table 1 and Figure S1). Note that $[Fe_4L_6]^{4-}$ can be crystallized in the $Fd\bar{3}$ space group, in which all facets are capped by less sterically hindering $[Fe(H_2O)_6]^{2+}$ cations, as compared to $(C(NH_2)_3)^+$.[42] The angle θ in $(Fe(H_2O)_6)_2[(X)Fe_4L_6]$, where X denotes an unidentified guest molecule, is 87.0(5)° (Table 1), well within the range of values for **1**−**7**. The larger θ in $(Fe(H_2O)_6)_2[(X)Fe_4L_6]$ is likely responsible for its larger internal volume,[42] despite the shorter M−M distance than those in **1** and **4** (Figure 2). The above discussions suggest that the desired all-facet-capped structure is not limited to the combination of $Co_nFe_{4-n}L_6$ and $(C(NH_2)_3)^+$. Such tunability is particularly important to design morphology and permanent porosity in future studies. Through the above systematic structural analysis, we can conclude that θ being in the range of 86−91° is the criterion for $[M_4L_6]^{4-}$ capsules to afford similar isostructural materials, assisted by C_3-symmetric H-bonding cations.

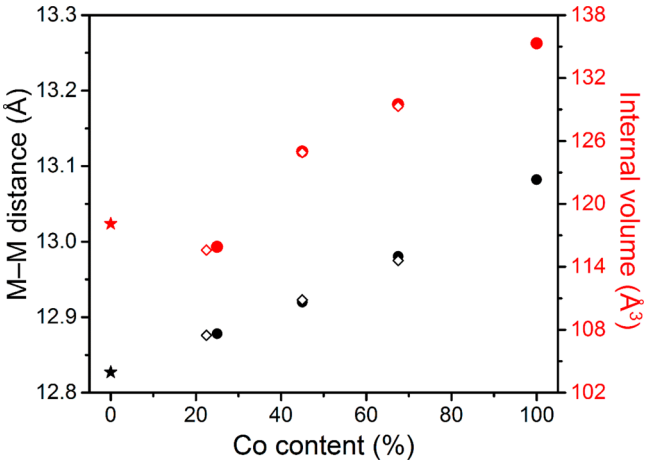

Figure 2. Summary of intramolecular metal−metal distances (black) and internal volumes (red) with respect to Co content in $[Co_nFe_{4-n}L_6]$ cages. Stars represent data from reported $(Fe(H_2O)_6)_2[(X)Fe_4L_6]$,[42] where X stands for an undefined guest molecule. Empty diamonds and solid circles represent data from compounds **1**−**3** (guest-free) and **4**−**7** (Xe-encapsulated), respectively.

To probe the homogeneity of Fe and Co contents in the crystalline sorbents, representative elemental analyses using SEM-EDX were carried out on a single crystal of **2** (Figure 3). The distributions of O, S, Fe, and Co, which are expected elements from the metal−organic capsules, are in great agreement with the defined area of the crystal in the SEM image. Superimposing the elemental maps for Fe and Co further confirms the homogeneous distribution of both Fe and Co (Figure 3, bottom right). Importantly, the abundance of Fe and Co, as determined by the EDX spectrum (Figure S2 and

https://doi.org/10.1021/acs.jpcc.3c02054
J. Phys. Chem. C 2023, 127, 13810−13816

Table 1. Summary of θ in Relevant $M^{II}_4L_6$ Structures[a]

	1	2[a]	3[a]	4	5[a]	6	7[b]	$(C(NH_2)_3)_4[Fe_4L_6]$[c]	$(Fe(H_2O)_6)_2[(X)Fe_4L_6]$[d]
θ (deg)	86.3(1)	86.2(1)	89.1(1)	86.9(1)	88.3(1)	89.9(1)	90.4(7)	95.5(2)/88.6(2)	87.0(5)

[a]Superscripts a, b, c, and d indicate statistics that are obtained by analyzing structures reported in refs 41, 40, 50, and 42, respectively. The letter "X" in [d] denotes an unidentified guest molecule.

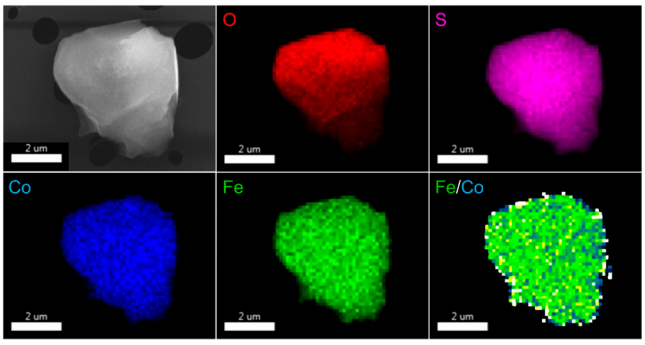

Figure 3. EDX analyses of a crystal of **2** that was adhered to an Al sample holder. Top left: SEM image of a crystal. EDX mapping for O (top middle), S (top right), Co (bottom left), Fe (bottom middle), and superimposed Fe and Co (bottom right), with each element monitored at its $K_{\alpha 1}$ wavelength.

Table S2) suggests a 1:1 Fe:Co ratio, which is well consistent with the bulk Fe:Co ratio determined by ICP-OES. The combined elemental analyses for bulk material and single crystals indicate that the guanidinium-assisted crystallization of the capsules did not induce microphase separation.

The thermal stabilities of sorbents and the encapsulated xenon atom were investigated by thermogravimetric analyses coupled with gas-phase mass spectrometry (TGA-MS). For guest-free compounds **1**−**3**, as temperatures increase from 303 to 423 K, the sample weights drop to ∼92% with concomitant release of crystallizing H_2O, as evidenced by the rising MS signal at m/z = 18. The sample weights then stay constant up to ∼593 K, beyond which two consecutive reductions in weight occur, both of which are accompanied by the release of H_2O and CO_2, as indicated in the MS chromatographs monitored at m/z = 18 and 44, respectively (Figures S3−S5). Because the experiments were conducted in an inert atmosphere of He, the releases of H_2O and CO_2 that occurred above 593 K are attributed to intramolecular degradation of the materials, likely caused by reduction of sulfonate groups and oxidation of the aryl linkers. For xenon-trapped compounds **4**−**7**, the release of crystallizing H_2O and oxidative degradation-generated CO_2 and H_2O occur at similar temperatures as **1**−**3** (Figures S6−S9). In addition, the sample weights reduce subtly by 2.0−3.5% over the range of 393−573 K, with concomitant rising MS signal at m/z = 131, indicating the release of encapsulated xenon (Figure 4). Note that the weight percent of xenon in the generic formula $(C(NH_2)_3)_4[(Xe)Co_nFe_{4-n}L_6]$ is ∼3.6%, which closely resembles the experimental reduction in mass due to the release of xenon. Particularly in the case of **4**, a significant amount of Xe remains encapsulated until the oxidative degradation of the material (Figure 4, bottom plot). The mean dissociation temperatures, T_m, at which 50% of xenon was released, are 425, 464, 515, and 561 K for **7**, **6**, **5**, and **4**, respectively. The T_m values are empirically proportional to the Fe content. The trend of increasing T_m for Xe-encapsulated compounds **7**−**4** predicts an even higher T_m for the hypothetical $Fd\bar{3}$ phase of $(C(NH_2)_3)_4[(Xe)Fe_4L_6]$ (all facets are capped), which we are currently unable to synthesize. However, the design strategy of considering θ and other combinations of metal centers and H-bond-donating cations may afford even more tunable Xe sorbents with higher T_m. Note that the T_m of 561 K for **4** is comparable to the T_m for the xenon-encapsulated complex of

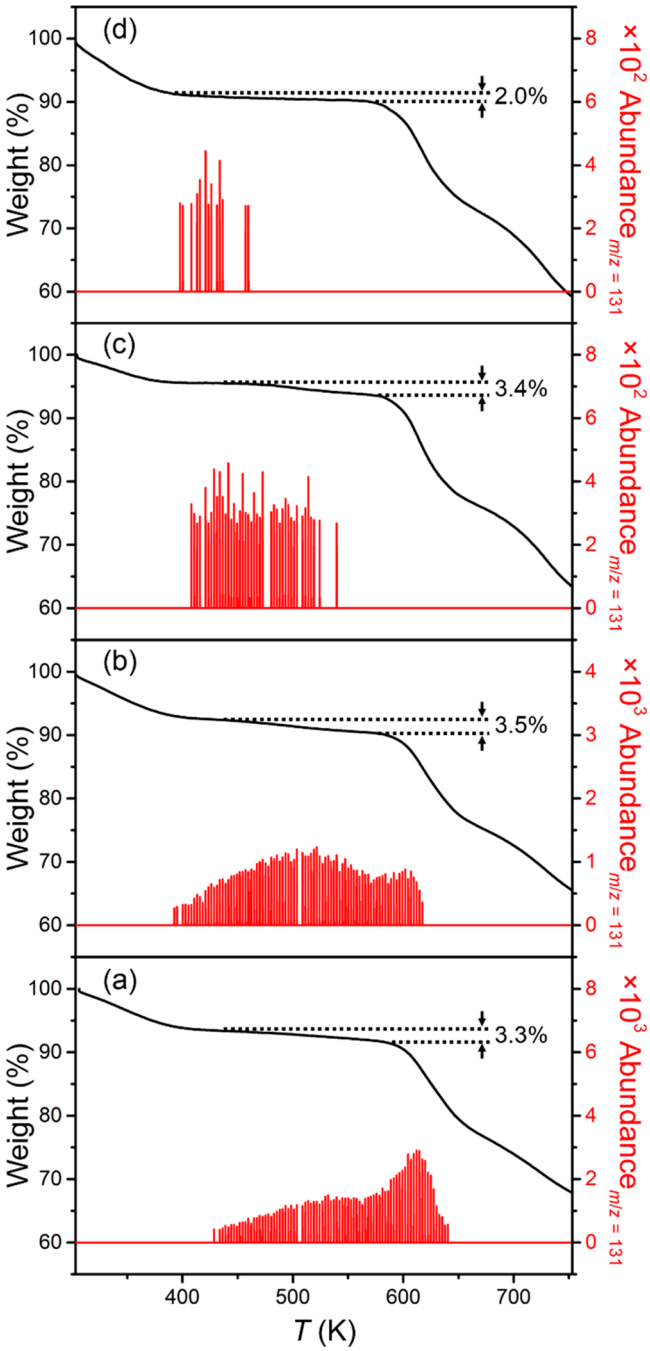

Figure 4. Summary of TGA-MS plots for (a) **4**, (b) **5**, (c) **6**, and (d) **7**. Black and red lines represent the thermogravimetric trace and the chromatograph monitored at m/z = 131, respectively.

https://doi.org/10.1021/acs.jpcc.3c02054
J. Phys. Chem. C 2023, 127, 13810−13816

cryptophane-111, despite **4** having nearly twice the internal volume.[34] The association constant for xenon for the smallest member of $[M_4L_6]^{4-}$, $[Fe_4L_6]^{4-}$, was reported to be 16 M^{-1} in D_2O,[39] which was over 1000-fold weaker than the one for a water-soluble derivative of cryptophane-111, $K = 2.9(2) \times 10^4$ M^{-1}. Therefore, the high T_m in **4** and the tunable dissociations of xenon in **4**–**7** are more likely attributed to tunable kinetic stabilization induced by the H-bond network.

CONCLUSIONS

The foregoing data demonstrate the tunable thermal dissociation of xenon in heterobimetallic Co_nFe_{4-n} molecular sorbents. Structural and elemental analyses in the solid state reveal the presence and absence of xenon, the incremental expansions/contractions of the $[M_4L_6]^{4-}$ capsules, and the homogeneous distribution of both Fe^{II} and Co^{II}. The dihedral angle θ, which bridges two neighboring sulfonate groups, dictates the formation of the desired face-centered cubic phase. Such criteria will help in guiding future crystal engineering by using $[M_4L_6]^{4-}$ capsules. The dissociation temperatures of the encapsulated xenon are highly tunable, ranging from 425 K in **7** to 561 K in **4**, which is nearly 400 K higher than the boiling point of xenon. Unlike the extreme confinement observed in cryptophane-111, the volume of the internal cavity in **4** is nearly twice that of cryptophane-111.[34] Previous solution-state studies on $[Co_nFe_{4-n}L_6]^{4-}$ capsules revealed that xenon affinities were significantly lower, and the xenon exchange rates were faster than measured for cryptophane-111.[39−41] Both factors are anticipated to promote xenon release. Hence, the stable and tunable entrapment of xenon in **4**–**7** is attributed to the physical barrier created by the guanidinium-induced H-bond networks.

ASSOCIATED CONTENT

Supporting Information

The Supporting Information is available free of charge at https://pubs.acs.org/doi/10.1021/acs.jpcc.3c02054.

Crystallographic data for **1**, **4**, and **6**, summary of dihedral angles, EDX spectra, TGA data for all compounds, and additional references (PDF)

Crystallographic data for **1** (CIF)

Crystallographic data for **4** (CIF)

Crystallographic data for **6** (CIF)

AUTHOR INFORMATION

Corresponding Author

Ivan J. Dmochowski − *Department of Chemistry, University of Pennsylvania, Philadelphia, Pennsylvania 19104−6323, United States;* orcid.org/0000-0001-7162-1347; Email: ivandmo@sas.upenn.edu

Author

Kang Du − *Department of Chemistry, University of Pennsylvania, Philadelphia, Pennsylvania 19104−6323, United States;* orcid.org/0000-0001-9947-2320

Complete contact information is available at: https://pubs.acs.org/10.1021/acs.jpcc.3c02054

Notes

The authors declare no competing financial interest.

ACKNOWLEDGMENTS

This work was supported by NIH Grant R35-GM-131907 to I.J.D. The authors gratefully acknowledge partial support of this research by NSF through the University of Pennsylvania Materials Research Science and Engineering Center (Grant DMR-1720530). K.D. was supported by the University of Pennsylvania. We thank Drs. Patrick J. Carroll and Michael R. Gau for insightful discussions on X-ray structural analysis and Dr. David R. Vann for assistance with ICP-OES experiments. EDX characterization carried out at the Singh Center for Nanotechnology is supported by the NSF National Nanotechnology Coordinated Infrastructure Program under Grant NNCI-2025608. TGA-MS instrumentation at IMSERC Physical Characterization Facility at Northwestern University is supported by the Soft and Hybrid Nanotechnology Experimental (SHyNE) Resource (Grant NSF ECCS-2025633) and Northwestern University.

REFERENCES

(1) Cullen, S. C.; Eger, E. I.; Cullen, B. F.; Gregory, P. Observations on the Anesthetic Effect of the Combination of Xenon and Halothane. *Anesthesiology* **1969**, *31*, 305−309.

(2) Cullen, S. C.; Gross, E. G. The Anesthetic Properties of Xenon in Animals and Human Beings, with Additional Observations on Krypton. *Science* **1951**, *113*, 580−582.

(3) Lassen, N. A.; Henriksen, L.; Holm, S.; Barry, D. I.; Paulson, O. B.; Vorstrup, S.; Rapin, J.; le Poncin-Lafitte, M.; Moretti, J. L.; Askienazy, S.; Raynaud, C. Cerebral Blood-Flow Tomography: Xenon-133 Compared with Isopropyl-Amphetamine-Iodine-123: Concise Communication. *J. Nucl. Med.* **1983**, *24*, 17−21.

(4) Mugler, J. P.; Driehuys, B.; Brookeman, J. R.; Cates, G. D.; Berr, S. S.; Bryant, R. G.; Daniel, T. M.; de Lange, E. E.; Downs, J. H.; Erickson, C. J.; et al. MR Imaging and Spectroscopy Using Hyperpolarized 129Xe Gas: Preliminary Human Results. *Magn. Reson. Med.* **1997**, *37*, 809−815.

(5) Kong, X.; Sheng, H. X.; Lu, G. M.; Meinel, F. G.; Dyer, K. T.; Schoepf, U. J.; Zhang, L. J. Xenon-Enhanced Dual-Energy CT Lung Ventilation Imaging: Techniques and Clinical Applications. *Am. J. Roentgenol.* **2014**, *202*, 309−317.

(6) Patterson, M. Ion Propulsion, 2016. National Aeronautics and Space Administration Web site. https://www.nasa.gov/centers/glenn/about/fs21grc.html (accessed March 28, 2020).

(7) Hwang, S.-C.; Lein, R. D.; Morgan, D. A. Noble Gases. *Kirk-Othmer Encyclopedia of Chemical Technology* [Online]; Wiley & Sons: New York, Posted August 19, 2005.

(8) Kerry, F. G. *Industrial Gas Handbook: Gas Separation and Purification*; CRC Press: Boca Raton, FL, 2007.

(9) Fontaine, J. P.; Pointurier, F.; Blanchard, X.; Taffary, T. Atmospheric Xenon Radioactive Isotope Monitoring. *J. Environ. Radioact.* **2004**, *72*, 129−135.

(10) Jubin, R. T.; Soelberg, N. R.; Strachan, D. M.; Ilas, G. Fuel Age Impacts on Gaseous Fission Product Capture During Separations; Report No. FCR&D-SWF-2012-000331; Oak Ridge National Laboratory: Oak Ridge, TN, 2012.

(11) Kitani, S.; Takada, J. Adsorption of Krypton and Xenon on Various Adsorbents. *J. Nucl. Sci. Technol.* **1965**, *2*, 51−56.

(12) Kuznetsova, A.; Yates, J. T.; Liu, J.; Smalley, R. E. Physical Adsorption of Xenon in Open Single Walled Carbon Nanotubes: Observation of a Quasi-One-Dimensional Confined Xe Phase. *J. Chem. Phys.* **2000**, *112*, 9590−9598.

(13) Babaa, M. R.; Stepanek, I.; Masenelli-Varlot, K.; Dupont-Pavlovsky, N.; McRae, E.; Bernier, P. Opening of Single-Walled Carbon Nanotubes: Evidence Given by Krypton and Xenon Adsorption. *Surf. Sci.* **2003**, *531*, 86−92.

(14) Jalili, S.; Majidi, R. Study of Xe and Kr Adsorption on Open Single-Walled Carbon Nanotubes Using Molecular Dynamics Simulations. *Physica E* **2007**, *39*, 166−170.

(15) Kuznicki, S. M.; Ansón, A.; Koenig, A.; Kuznicki, T. M.; Haastrup, T.; Eyring, E. M.; Hunter, D. Xenon Adsorption on Modified ETS-10. *J. Phys. Chem. C* **2007**, *111*, 1560−1562.
(16) Daniel, C.; Elbaraoui, A.; Aguado, S.; Springuel-Huet, M.-A.; Nossov, A.; Fontaine, J.-P.; Topin, S.; Taffary, T.; Deliere, L.; Schuurman, Y.; et al. Xenon Capture on Silver-Loaded Zeolites: Characterization of Very Strong Adsorption Sites. *J. Phys. Chem. C* **2013**, *117*, 15122−15129.
(17) Feng, X.; Zong, Z.; Elsaidi, S. K.; Jasinski, J. B.; Krishna, R.; Thallapally, P. K.; Carreon, M. A. Kr/Xe Separation Over a Chabazite Zeolite Membrane. *J. Am. Chem. Soc.* **2016**, *138*, 9791−9794.
(18) Parkes, M. V.; Staiger, C. L.; Perry, J. J.; Allendorf, M. D.; Greathouse, J. A. Screening Metal-Organic Frameworks for Selective Noble Gas Adsorption in Air: Effect of Pore Size and Framework Topology. *Phys. Chem. Chem. Phys.* **2013**, *15*, 9093−9106.
(19) Liu, J.; Fernandez, C. A.; Martin, P. F.; Thallapally, P. K.; Strachan, D. M. A Two-Column Method for the Separation of Kr and Xe from Process Off-Gases. *Ind. Eng. Chem. Res.* **2014**, *53*, 12893−12899.
(20) Kapelewski, M. T.; Oktawiec, J.; Runčevski, T.; Gonzalez, M. I.; Long, J. R. Separation of Xenon and Krypton in the Metal-Organic Frameworks M2(m-dobdc) (M=Co, Ni). *Isr. J. Chem.* **2018**, *58*, 1138−1143.
(21) Li, L.; Guo, L.; Zhang, Z.; Yang, Q.; Yang, Y.; Bao, Z.; Ren, Q.; Li, J. A Robust Squarate-Based Metal-Organic Framework Demonstrates Record-High Affinity and Selectivity for Xenon Over Krypton. *J. Am. Chem. Soc.* **2019**, *141*, 9358−9364.
(22) Banerjee, D.; Simon, C. M.; Elsaidi, S. K.; Haranczyk, M.; Thallapally, P. K. Xenon Gas Separation and Storage Using Metal-Organic Frameworks. *Chem* **2018**, *4*, 466−494.
(23) Chen, X.; Plonka, A. M.; Banerjee, D.; Krishna, R.; Schaef, H. T.; Ghose, S.; Thallapally, P. K.; Parise, J. B. Direct Observation of Xe and Kr Adsorption in a Xe-Selective Microporous Metal-Organic Framework. *J. Am. Chem. Soc.* **2015**, *137*, 7007−7010.
(24) Brekalo, I.; Deliz, D.; Barbour, L. J.; Ward, M. D.; Friščić, T.; Holman, K. T. Microporosity of a Guanidinium Organodisulfonate Hydrogen-Bonded Framework,. *Angew. Chem., Int. Ed.* **2020**, *59*, 1997−2002.
(25) Meek, S. T.; Teich-McGoldrick, S. L.; Perry, J. J.; Greathouse, J. A.; Allendorf, M. D. Effects of Polarizability on the Adsorption of Noble Gases at Low Pressures in Monohalogenated Isoreticular Metal-Organic Frameworks. *J. Phys. Chem. C* **2012**, *116*, 19765−19772.
(26) Bloch, E. D.; Queen, W. L.; Krishna, R.; Zadrozny, J. M.; Brown, C. M.; Long, J. R. Hydrocarbon Separations in a Metal-Organic Framework with Open Iron(II) Coordination Sites. *Science* **2012**, *335*, 1606−1610.
(27) Barnett, B. R.; Gonzalez, M. I.; Long, J. R. Recent Progress Towards Light Hydrocarbon Separations Using Metal-Organic Frameworks. *Trends Chem.* **2019**, *1*, 159−171.
(28) Deliere, L.; Topin, S.; Coasne, B.; Fontaine, J.-P.; De Vito, S.; Den Auwer, C.; Solari, P. L.; Daniel, C.; Schuurman, Y.; Farrusseng, D. Role of Silver Nanoparticles in Enhanced Xenon Adsorption Using Silver-Loaded Zeolites. *J. Phys. Chem. C* **2014**, *118*, 25032−25040.
(29) Deliere, L.; Coasne, B.; Topin, S.; Gréau, C.; Moulin, C.; Farrusseng, D. Breakthrough in Xenon Capture and Purification Using Adsorbent-Supported Silver Nanoparticles. *Chem. J. Euro.* **2016**, *22*, 9660−9666.
(30) Bondi, A. van der Waals Volumes and Radii. *J. Phys. Chem.* **1964**, *68*, 441−451.
(31) Chen, L.; Reiss, P. S.; Chong, S. Y.; Holden, D.; Jelfs, K. E.; Hasell, T.; Little, M. A.; Kewley, A.; Briggs, M. E.; Stephenson, A.; et al. Separation of Rare Gases and Chiral Molecules by Selective Binding in Porous Organic Cages. *Nat. Mater.* **2014**, *13*, 954−960.
(32) Takamizawa, S.; Akatsuka, T.; Ueda, T. Gas-Conforming Transformability of an Ionic Single-Crystal Host Consisting of Discrete Charged Components. *Angew. Chem., Int. Ed.* **2008**, *47*, 1689−1692.
(33) Taratula, O.; Hill, P. A.; Khan, N. S.; Carroll, P. J.; Dmochowski, I. J. Crystallographic Observation of 'Induced Fit' in a Cryptophane Host-Guest Model System. *Nat. Commun.* **2010**, *1*, 148−154.
(34) Joseph, A. I.; Lapidus, S. H.; Kane, C. M.; Holman, K. T. Extreme Confinement of Xenon by Cryptophane-111 in the Solid-State. *Angew. Chem., Int. Ed.* **2015**, *54*, 1471−1475.
(35) Ilczyszyn, M.; Selent, M.; Ilczyszyn, M. M. Participation of Xenon Guest in Hydrogen Bond Network of β-Hydroquinone Crystal. *J. Phys. Chem. A* **2012**, *116*, 3206−3214.
(36) Kane, C. M.; Banisafar, A.; Dougherty, T. P.; Barbour, L. J.; Holman, K. T. Enclathration and Confinement of Small Gases by the Intrinsically 0D Porous Molecular Solid, Me,H, $SiMe_2$. *J. Am. Chem. Soc.* **2016**, *138*, 4377−4392.
(37) He, S.; Biedermann, F.; Vankova, N.; Zhechkov, L.; Heine, T.; Hoffman, R. E.; DeSimone, A.; Duignan, T. T.; Nau, W. M. Cavitation Energies Can Outperform Dispersion Interactions. *Nat. Chem.* **2018**, *10*, 1252−1257.
(38) Egleston, B. D.; Luzyanin, K. V.; Brand, M. C.; Clowes, R.; Briggs, M. E.; Greenaway, R. L.; Cooper, A. I. Controlling Gas Selectivity in Molecular Porous Liquids by Tuning the Cage Window Size. *Angew. Chem., Int. Ed.* **2020**, *59*, 7362−7366.
(39) Roukala, J.; Zhu, J.; Giri, C.; Rissanen, K.; Lantto, P.; Telkki, V.-V. Encapsulation of Xenon by a Self-Assembled Fe_4L_6 Metallosupramolecular Cage. *J. Am. Chem. Soc.* **2015**, *137*, 2464−2467.
(40) Du, K.; Zemerov, S. D.; Hurtado Parra, S.; Kikkawa, J. M.; Dmochowski, I. J. Paramagnetic Organocobalt Capsule Revealing Xenon Host-Guest Chemistry. *Inorg. Chem.* **2020**, *59*, 13831−13844.
(41) Du, K.; Zemerov, S. D.; Carroll, P. J.; Dmochowski, I. J. Paramagnetic Shifts and Guest Exchange Kinetics in Co_nFe_{4-n} Metal-Organic Capsules. *Inorg. Chem.* **2020**, *59*, 12758−12767.
(42) Ronson, T. K.; Giri, C.; Kodiah Beyeh, N.; Minkkinen, A.; Topić, F.; Holstein, J. J.; Rissanen, K.; Nitschke, J. R. Size-Selective Encapsulation of Hydrophobic Guests by Self-Assembled M_4L_6 Cobalt and Nickel Cages. *Chem. - Eur. J.* **2013**, *19*, 3374−3382.
(43) *SAINT*, version 8.34A; Bruker-AXS: Madison, WI, 2014.
(44) Sheldrick, G. M. *SADABS*, version 2.03; Bruker Analytical X-Ray Systems, Inc.: Madison, WI, 2000.
(45) *APEX3*, version 2018.1-0; Bruker-AXS: Madison, WI, 2014.
(46) Sheldrick, G. M. SHELXT-Integrated Space-Group and Crystal-Structure Determination. *Acta Crystallogr., Sect. A: Found. Adv.* **2015**, *71*, 3−8.
(47) Sheldrick, G. M. *SHELXTL*, version 6.12; Bruker Analytical X-Ray Systems, Inc.: Madison, WI, 2000.
(48) Dolomanov, O. V.; Bourhis, L. J.; Gildea, R. J.; Howard, J. A. K.; Puschmann, H. OLEX2: A Complete Structure Solution, Refinement and Analysis Program. *J. Appl. Crystallogr.* **2009**, *42*, 339−341.
(49) Spek, A. PLATON SQUEEZE: A Tool for the Calculation of the Disordered Solvent Contribution to the Calculated Structure Factors. *Acta Cryst. C* **2015**, *71*, 9−18.
(50) Zarra, S.; Smulders, M. M. J.; Lefebvre, Q.; Clegg, J. K.; Nitschke, J. R. Guanidinium Binding Modulates Guest Exchange within an $[M_4L_6]$ Capsule. *Angew. Chem., Int. Ed.* **2012**, *51*, 6882−6885.

https://doi.org/10.1021/acs.jpcc.3c02054
J. Phys. Chem. C 2023, 127, 13810−13816